Journal of Quantitative Spectroscopy & Radiative Transfer 111 (2010) 529–539

Contents lists available at ScienceDirect

Journal of Quantitative Spectroscopy & Radiative Transfer

journal homepage: www.elsevier.com/locate/jqsrt

Reflection models for soil and vegetation surfaces from multiple-viewing angle photopolarimetric measurements

Pavel Litvinov [a,*], Otto Hasekamp [a], Brian Cairns [b], Michael Mishchenko [b]

[a] SRON Netherlands Institute for Space Research, Sorbonnelaan 2, 3584 CA Utrecht, The Netherlands
[b] NASA Goddard Institute for Space Studies, 2880 Broadway, New York, NY 10025, USA

ARTICLE INFO

Article history:
Received 1 July 2009
Received in revised form
25 September 2009
Accepted 2 November 2009

Keywords:
Bidirectional reflectance matrix (BDRM)
Bidirectional reflection function (BDRF)
Bidirectional polarization distribution function (BPDF)
Reflection models
Land surfaces
Research scanning polarimeter (RSP)

ABSTRACT

The reflection properties of soil and vegetation surfaces have been investigated using airborne photopolarimetric data from the research scanning polarimeter (RSP). For both surface types, it was found that the ratios of total reflectances taken at two different wavelengths from visible and short-wave infrared channels are the same for different illumination and scattering geometries, and in general independent of the scattering angle. From an analysis of the angular and spectral dependencies of the intensity and polarization, we show that the modeled total and polarized reflectances can be expressed in the same form both for soil and vegetation surfaces, namely, as the product of geometrical scattering term depending only on illumination and viewing angles, and a term that varies solely with wavelength and scattering angle.

© 2009 Elsevier Ltd. All rights reserved.

1. Introduction

The bidirectional reflection matrix (BDRM) describes intrinsic reflectance properties of surfaces. It provides a relation between the Stokes parameters of scattered and incident radiation fields. To describe separately the surface contribution into intensity and polarization characteristics of scattered radiation the bidirectional reflection function (BDRF) and bidirectional polarization distribution function (BPDF) are used instead of the BDRM. On the basis of knowledge of the BDRM surface properties can be retrieved from satellite measurements [1–3]. Moreover, accurate models of BDRF and BPDF at visible and infrared wavelength are required for retrieval of aerosol properties over land surfaces.

In general the BDRM can be expressed as follows:

$$\mathbf{R}_{surf}(\lambda, \mathbf{n}_v, \mathbf{n}_{inc}) = \mathbf{R}_1(\lambda, \mathbf{n}_v, \mathbf{n}_{inc}) + \mathbf{R}_{mult}(\lambda, \mathbf{n}_v, \mathbf{n}_{inc}), \quad (1)$$

where the matrix $\mathbf{R}_1(\lambda, \mathbf{n}_v, \mathbf{n}_{inc})$ corresponds to single scattering and $\mathbf{R}_{mult}(\lambda, \mathbf{n}_v, \mathbf{n}_{inc})$ takes into account multiple scattering in a medium (λ is the wavelength of incident radiation, $\mathbf{n}_v$ and $\mathbf{n}_{inc}$ are the unit vectors in the direction of viewing and incidence, respectively). In application to soil and vegetation surfaces $\mathbf{R}_1(\lambda, \mathbf{n}_v, \mathbf{n}_{inc})$ may be considered as a reflection matrix from the separate leaves, or as a reflection matrix from the randomly oriented soil particles [1–8], whereas $\mathbf{R}_{mult}(\lambda, \mathbf{n}_v, \mathbf{n}_{inc})$ describes multiple scattering between leaves or soil particles.

In the case when it is necessary to take into account the multiple scattering contribution, physical models for $\mathbf{R}_{surf}(\lambda, \mathbf{n}_v, \mathbf{n}_{inc})$ can be very complicated or too time consuming to be used in inverse scattering schemes [3,9,10]. Some models of the BDRM for vegetation and soil are based on the scalar radiative transfer theory, consider the contribution of $\mathbf{R}_{mult}(\lambda, \mathbf{n}_v, \mathbf{n}_{inc})$ approximately or as a Lambertian term, which contributes just to intensity

* Corresponding author.
E-mail addresses: P.Litvinov@sron.nl, PVLitvinov@mail.ru (P. Litvinov).

0022-4073/$ - see front matter © 2009 Elsevier Ltd. All rights reserved.
doi:10.1016/j.jqsrt.2009.11.001

(matrix element $R_{11}(\lambda, \mathbf{n}_v, \mathbf{n}_{inc})$) but not to polarization and does not depend on the illumination and scattering conditions (see, for example, [11–15]). In particular, in the problem of aerosol properties retrievals over land the semi-empirical models of BDRF and BPDF for earth surfaces are usually used [14–22]. Within these models surface reflectance is described by the kernel-driven models [14–17], whereas polarization of radiation reflected from natural surfaces is usually considered as spectrally independent in the visible and infrared regions and is described by models based on the assumption of single Fresnel reflection from the surface facets (see, for example, [1,18–22]). These semi-empirical BDRF and BPDF models are not related to each other. In particular, strong spectral dependence of the total reflectance both for soil and vegetation surfaces cannot be explained just by single Fresnel reflection from surfaces, and volume scattering inside of leaves and soil particles must be taken into account (see, for example, [7,8]). It is still a question how important the volume scattering may be for polarized reflectance.

The research scanning polarimeter (RSP) [23] provides an unique opportunity to investigate the directional and polarization properties of surface reflection. It is an airborne prototype of the aerosol polarimetry sensor (APS) [24] to be launched on the NASA Glory mission in 2010, which measures intensity and polarization at multiple viewing angles in spectral bands ranging from the blue to the short-wave infrared. During the ALIVE (Aerosol Lidar Validation Experiment) measurement campaign in Oklahoma (USA, Southern Great Plains) in September 2005, some flights have been performed at low altitude over land. The aim of this paper is to investigate the directional and polarization properties of reflection by soil and vegetated surfaces making use of these low altitude RSP measurements. Here, we compare RSP measurements with theoretical models based on vector radiative transfer theory for discrete random media and the Kirchhoff approximation in the geometric optics limit for Gaussian rough surfaces (Fresnel's reflection from Gaussian rough surfaces). Furthermore, we present a simple general form for models of total and polarized reflectance from soil and vegetated surfaces and draw conclusions about the dependence of the model parameters on the wavelength.

2. The research scanning polarimeter (RSP)

2.1. RSP data description

RSP measures intensity and linear polarization characteristics at viewing zenith angles in the range $\pm 60^\circ$ in nine spectral bands in the range 410–2250 nm. As it was mentioned above, we used the RSP data obtained during the ALIVE measurement campaign performed in Oklahoma [25]. There are several flights in the ALIVE campaign with measurements at low altitude over land (about 200–600 m). These measurements provide good opportunity for investigating reflection properties of the Earth surface.

Table 1 contains a description of the flights that were used in this study. The flights were carried out over the same area (see Fig. 1) at different times during the same day and at similar weather conditions. Thus the data for these flights are obtained for different illumination and scattering geometries and related in average to the same types of soil and vegetation surfaces.

Soil and other nonvegetated surfaces have much smaller spectral contrast between the 'red' and 'near-infrared' bands. Following [25,26] we used the Atmospherically Resistant Vegetation Index (*ARVI*) to distinguish soil and vegetation types of surfaces. The *ARVI* can be defined as [25,26]

$$ARVI = \frac{R_I^{(NIR)} - R_I^{(rb)}}{R_I^{(NIR)} + R_I^{(rb)}}, \tag{2}$$

$$R_I^{rb} = R_I^{(red)} - \gamma(R_I^{(blue)} - R_I^{(red)}), \tag{3}$$

where $R_I^{(NIR)}$, $R_I^{(red)}$ and $R_I^{(blue)}$ are the total reflectances (see Appendix A for the definition) in the 'near-infrared' ($\lambda = 865$), 'red' ($\lambda = 670$) and 'blue' ($\lambda = 470$) spectral bands, respectively, γ is a parameter that depends on aerosol type (following [25], we used $\gamma = 0.9$).

The data with $-0.25 < ARVI < 0.075$ and $0.375 < ARVI < 0.775$ were classified as 'soil' and 'vegetation', respectively. A detailed description of splitting the data

Table 1
Flights considered in the paper.

	Flight 1	Flight 2	Flight 3	Flight 4
Month, date and year	September 16, 2005	September 16, 2005	September 16, 2005	September 16, 2005
Time (UTC)	16:32:25	22:01:49	16:25:24	22:09:32
Average altitude over sea level (m)	510	942	640	476
Average solar zenith angle (ϑ_{sol}) (deg)	42.68	60.8	43.67	62
Average solar azimuth angle (φ_{sol}) (deg)	136.7	249.1	134.5	250.3
Average observation azimuth angle (φ_v') (deg)	90.75	227.3	271.2	46
Average *ARVI*, soil	0.033	0.024	0.031	–
Number of scans for averaging, soil	46–71	22–41	22–48	–
Average *ARVI*, vegetation	0.63	0.65	–	0.577
Number of scan for averaging, vegetation	59–85	11–31	–	9–21
Aerosol optical thickness at $\lambda = 670$ nm	0.039	0.046	0.039	0.038
Aerosol optical thickness at $\lambda = 1588.9$ nm	0.0075	0.01256	0.0075	0.0083
Aerosol optical thickness at $\lambda = 2264.38$ nm	0.0037	0.0075	0.0037	0.0046

into a 'soil' and 'vegetation' classes for the flights 1 and 4 from Table 1 is presented in [25]. Using this classification for each flight from Table 1, we averaged the intensity and polarization measurements over different realizations (scans) separately for soil and vegetation surfaces.

Figs. 2 and 3 contain an example of the angular dependencies of the total reflectance R_I and polarized reflectance R_P (see definitions in Appendix A) averaged over different scans of the flights 1 and 2 described in Table 1.

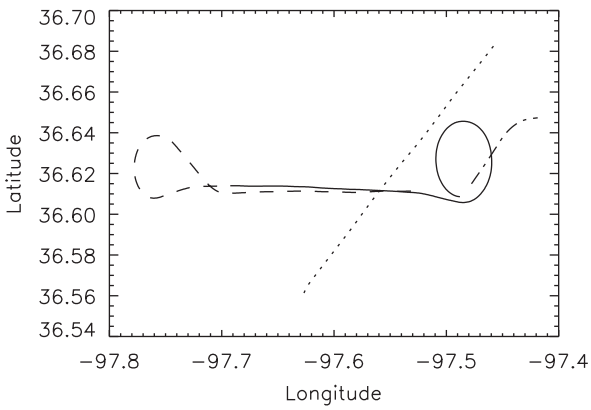

Fig. 1. Flights ground tracks. Solid, dotted, dashed and dash-dotted curves show tracks of the flights 1, 2, 3 and 4, respectively (see Table 1).

2.2. Atmospheric correction

For the analysis of R_I and R_P of soil and vegetation surfaces we chose the channel 4 ('red' band, $\lambda = 670$ nm) and the channels 7, 9 (two 'infrared' bands, $\lambda = 1588.86$ and 2264.38 nm), where aerosol optical thickness is small (see Table 1).

At RSP flight altitude, the reflection matrix for a coupled atmosphere–surface system can be written as [18]

$$\mathbf{R}^{atm}_{surf}(z, \mathbf{n}_v, \mathbf{n}_{inc}) = \mathbf{R}_{surf}(\mathbf{n}_v, \mathbf{n}_{inc})\exp(-\tau/\mu_{inc})\exp(-\tau_z/\mu_v) + \mathbf{R}'^{atm}_{surf}(z, \mathbf{n}_v, \mathbf{n}_{inc}). \quad (4)$$

Here $\mathbf{R}_{surf}(\mathbf{n}_v, \mathbf{n}_{inc})$ is the reflection matrix from the surface, τ is the atmospheric optical thickness, τ_z is the atmospheric optical thickness between the land surface and the airplane ($\tau = \tau_{aer} + \tau_{mol}$, τ_{aer} and τ_{mol} are aerosol and molecular optical thicknesses, respectively), $\mu_v = |\cos\vartheta_v|$, $\mu_{inc} = |\cos\vartheta_{inc}|$ (ϑ_v and ϑ_{inc} are viewing and solar zenith angles, respectively), $\mathbf{R}'^{atm}_{surf}(z, \mathbf{n}_v, \mathbf{n}_{inc})$ is the reflection matrix which takes into account single and multiple scattering in the atmosphere as well as scattering between the atmosphere and surface.

As one can see from Eq. (4), in order to obtain surface total reflectance R_I and surface polarized reflectance R_P from the RSP measurements, we need to estimate the term $\mathbf{R}'^{atm}_{surf}$. Hereto, we use a radiative transfer model for the coupled atmosphere–surface system [27,28], which

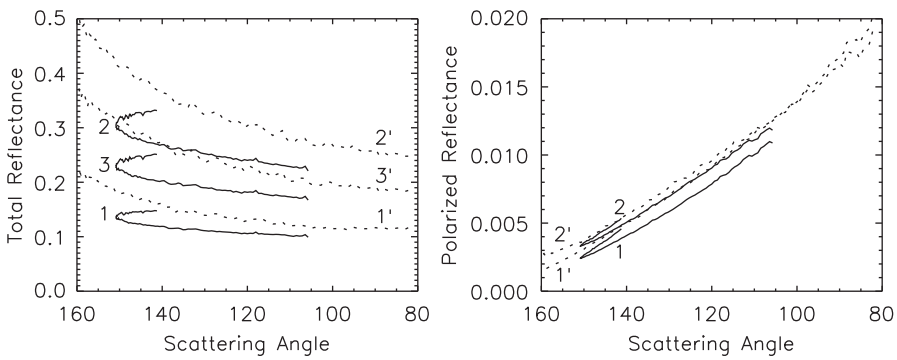

Fig. 2. Angular dependencies of averaged total reflectance and polarized reflectance for soil. The solid curves 1, 2, 3 correspond to the flight 1 from Table 1. The dotted curves 1′, 2′, 3′ correspond to the flight 2 from Table 1. The curves 1 and 1′ are obtained for $\lambda = 670$ nm (channel 4); 2 and 2′: for $\lambda = 1588.86$ nm (channel 7); 3 and 3′: for $\lambda = 2264.38$ nm (channel 9).

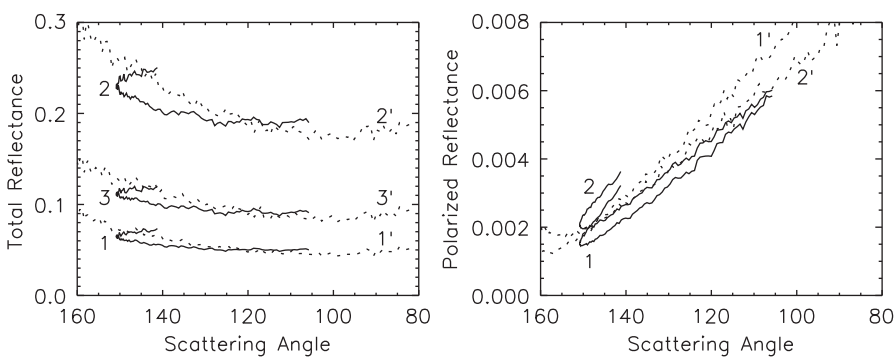

Fig. 3. The same dependencies as in Fig. 2 but for vegetation type of surface.

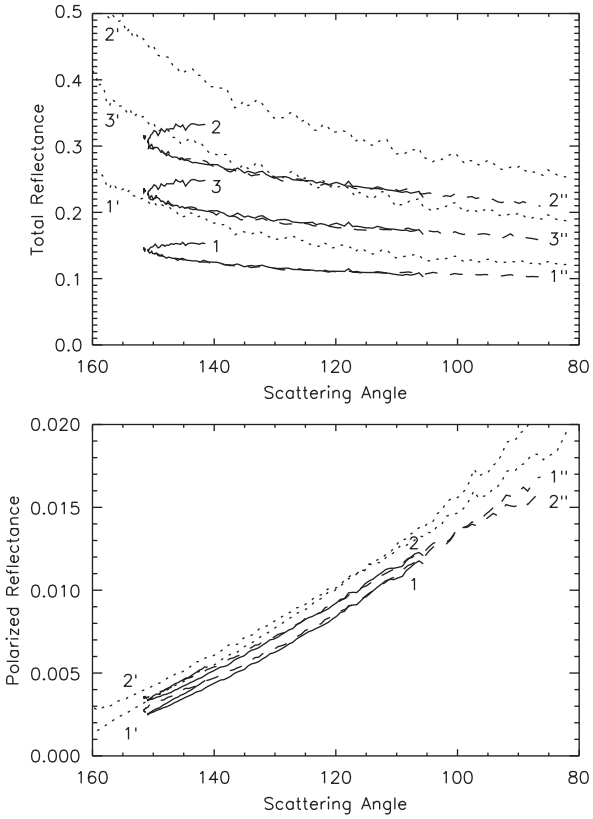

Fig. 4. Angular dependencies of corrected for atmosphere contribution averaged total reflectance and polarized reflectance for soil. The curves 1, 2, 3 correspond to the flight 1; 1′, 2′, 3′ correspond to the flight 2, and the curves 1″, 2″, 3″ correspond to the flight 3 from Table 1. The curves 1, 1′ and 1″ are obtained for $\lambda = 670$ nm (channel 4); 2, 2′ and 2″: for $\lambda = 1588.86$ nm (channel 7); 3, 3′ and 3″: for $\lambda = 2264.38$ nm (channel 9).

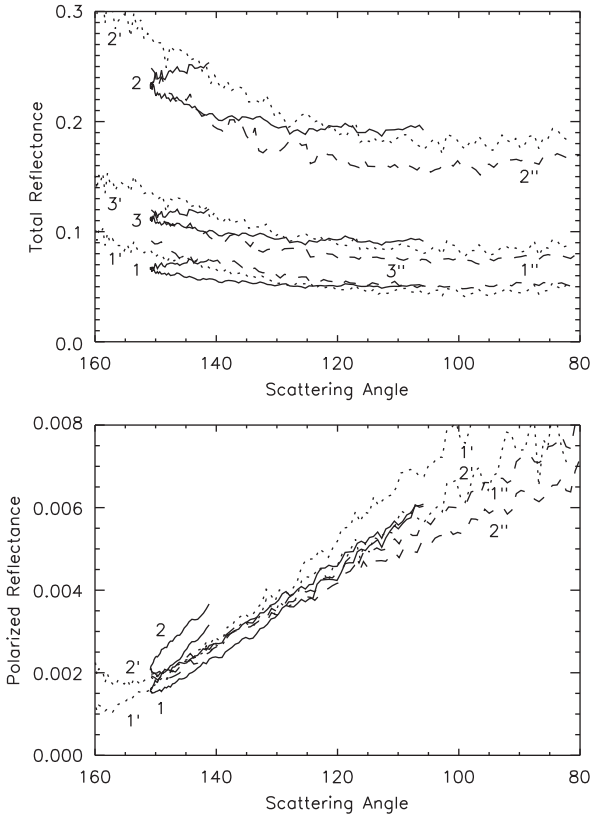

Fig. 5. The same dependencies as in Fig. 4 but for vegetation type of surface, and the curves 1″, 2″, 3″ correspond to the flight 4 from Table 1.

requires as input the aerosol optical thickness, single scattering albedo and scattering matrix. The values of τ_{aer} for different wavelengths were taken from an AERONET station in Oklahoma (The U.S. Southern Great Plains (SGP) Cloud and Radiation Testbed (CART) Site). The other aerosol parameters are taken from an aerosol model representative for a US background scenario taken from the ECHAM5-HAM model [29]. Also, we need a model that describes surface reflection. Here, we use for the total reflectance the model given by Rahman et al. [16], and for polarized reflectance a model based on the Kirchhoff approximation in geometrical optics limit for rough surfaces with Gaussian distribution of surface slopes [18]. The parameters of the BDRF and BPDF models were chosen such that they agree well with the RSP measurements. It is important to note that due to the small optical thickness in the red and short-wave infrared channels of RSP (see Table 1), the term $\mathbf{R}'^{atm}_{surf}$ is only marginally affected by particular choices of surface and aerosol models.

Figs. 4 and 5 show the angular dependencies of R_I and R_P for soil and vegetation surfaces after the atmospheric correction. As one can see, the correction is not considerable for the chosen channels. In the following section we consider surface R_I and R_P obtained under different illumination and scattering geometries to test theoretical models of the BDRF and BPDF for soil and vegetation types of terrestrial surfaces.

3. Testing BDRF and BPDF models

3.1. Theoretical analysis of BDRF and BPDF models

The reflection matrix $\mathbf{R}_{surf}(\lambda, \mathbf{n}_v, \mathbf{n}_{inc})$ can be written as [9,30]

$$\mathbf{R}_{surf}(\lambda, \mathbf{n}_v, \mathbf{n}_{inc}) = \mathbf{L}(\eta_v)\mathbf{R}'_{surf}(\lambda, \mathbf{n}_v, \mathbf{n}_{inc}, \vartheta)\mathbf{L}(\eta_{inc})f(\mathbf{n}_v, \mathbf{n}_{inc}). \quad (5)$$

Here $\mathbf{R}'_{surf}(\lambda, \mathbf{n}_v, \mathbf{n}_{inc}, \vartheta)$ is a wavelength dependent reflection matrix relating the Stokes parameters of scattered radiation to the Stokes parameters of incident radiation defined in the scattering plane, ϑ is the scattering angle, $\mathbf{L}(\eta_v)$ and $\mathbf{L}(\eta_{inc})$ are the Stokes rotation matrices for angles η_v and η_{inc} (see Appendix A) [9,30], $f(\mathbf{n}_v, \mathbf{n}_{inc})$ is a wavelength independent function of zenith incidence ϑ_{inc}, zenith viewing ϑ_v angles and the azimuth angles of incidence and viewing directions φ_{inc}, φ_v.

An important simplification of the BDRM is possible, if one assumes that the wavelength dependent matrix $\mathbf{R}'_{surf}$ in Eq. (5) only depends on the scattering angle ϑ. For example, in single scattering approximation just the matrix $\mathbf{R}_1(\lambda, \mathbf{n}_v, \mathbf{n}_{inc})$ is taken into account in Eq. (1). If the single scattering is produced by inhomogeneities

which are randomly oriented with respect to incident and scattered directions (for example, by chaotically oriented leaves for vegetation, by chaotically oriented nonspherical particles of soil, etc.) or by randomly oriented facets with Fresnel reflection, $\mathbf{R}_{surf}(\lambda, \mathbf{n}_v, \mathbf{n}_{inc})$ can be presented as [1,9,30]

$$\mathbf{R}_{surf}(\lambda, \mathbf{n}_v, \mathbf{n}_{inc}) = \mathbf{L}(\eta_v)\mathbf{F}(\lambda, \vartheta)\mathbf{L}(\eta_{inc})f(\mathbf{n}_v, \mathbf{n}_{inc}), \tag{6}$$

where $\mathbf{F}(\lambda, \vartheta)$ is the scattering matrix averaged over orientations of inhomogeneities (for facets with Fresnel reflection $\mathbf{F}(\lambda, \vartheta)$ is the Fresnel reflection matrix with the angles of incidence and reflection equal to $(\pi - \vartheta)/2$), and $f(\mathbf{n}_v, \mathbf{n}_{inc})$ is a wavelength independent function of the incident, viewing zenith angles and the azimuth angles of incidence and viewing directions. For random rough surfaces it may depend on properties of the surface, for example, on a probability density function for the slopes at the surface, and may contain also a shadowing function (see, for example, [1]).

Taking into account that $\mathbf{F}(\lambda, \vartheta)$ for chaotically oriented and mirror symmetric particles has a block-diagonal shape, the Stokes parameters I, Q and U of scattered radiation, normalized to the flux incident on a unit of a surface, can be written as (incident radiation is supposed to be unpolarized)

$$I_\lambda(\mathbf{n}_v, \mathbf{n}_{inc}) = R_{11}(\lambda, \mathbf{n}_v, \mathbf{n}_{inc}) = F_{11}(\lambda, \vartheta)f(\mathbf{n}_v, \mathbf{n}_{inc}), \tag{7}$$

$$Q_\lambda(\mathbf{n}_v, \mathbf{n}_{inc}) = R_{21}(\lambda, \mathbf{n}_v, \mathbf{n}_{inc}) = F_{21}(\lambda, \vartheta)\cos 2\eta_v f(\mathbf{n}_v, \mathbf{n}_{inc}), \tag{8}$$

$$U_\lambda(\mathbf{n}_v, \mathbf{n}_{inc}) = R_{31}(\lambda, \mathbf{n}_v, \mathbf{n}_{inc}) = F_{21}(\lambda, \vartheta)\sin 2\eta_v f(\mathbf{n}_v, \mathbf{n}_{inc}). \tag{9}$$

From Eqs. (7) to (9) one can write for the ratios of the Stokes parameters taken at two different wavelengths λ_1 and λ_2:

$$K_i(\lambda_1, \lambda_2, \vartheta) = \frac{I_{\lambda_1}(\mathbf{n}_v, \mathbf{n}_{inc})}{I_{\lambda_2}(\mathbf{n}_v, \mathbf{n}_{inc})} = \frac{F_{11}(\lambda_1, \vartheta)}{F_{11}(\lambda_2, \vartheta)}, \tag{10}$$

$$K_q(\lambda_1, \lambda_2, \vartheta) = \frac{Q_{\lambda_1}(\mathbf{n}_v, \mathbf{n}_{inc})}{Q_{\lambda_2}(\mathbf{n}_v, \mathbf{n}_{inc})} = \frac{F_{21}(\lambda_1, \vartheta)}{F_{21}(\lambda_2, \vartheta)}, \tag{11}$$

$$K_u(\lambda_1, \lambda_2, \vartheta) = \frac{U_{\lambda_1}(\mathbf{n}_v, \mathbf{n}_{inc})}{U_{\lambda_2}(\mathbf{n}_v, \mathbf{n}_{inc})} = \frac{F_{21}(\lambda_1, \vartheta)}{F_{21}(\lambda_2, \vartheta)}, \tag{12}$$

$$K_p(\lambda_1, \lambda_2, \vartheta) = \frac{\sqrt{Q_{\lambda_1}^2 + U_{\lambda_1}^2}}{\sqrt{Q_{\lambda_2}^2 + U_{\lambda_2}^2}} = \frac{F_{21}(\lambda_1, \vartheta)}{F_{21}(\lambda_2, \vartheta)}. \tag{13}$$

Thus if the reflection matrix can be presented in the form given by Eq. (6), the ratios of intensities (Eq. (10)) and polarization characteristics (Eqs. (11)–(13)) taken at two different wavelengths λ_1 and λ_2 depend just on the wavelengths and the scattering angle. Since different illumination and scattering conditions may give the same ϑ (see, for example, Figs. 4 and 5), the ratios (10)–(13) must be the same for different sets of ϑ_{inc}, ϑ_v, φ_{inc}, φ_v which give the same scattering angle ϑ. To demonstrate this we carried out calculations for two different illumination and scattering geometries.

Fig. 6 presents results of calculations of $K_i(\lambda_1, \lambda_2, \vartheta)$ and $K_p(\lambda_1, \lambda_2, \vartheta)$ for the illumination and scattering conditions of the flights 1 and 2 (see Table 1). The calculations are based on the Kirchhoff approximation in geometrical optics limit for rough surfaces with Gaussian distribution of surface slopes [18]. In this approximation just single scattering by facets with Fresnel reflection is taken into account. The refractive index m of the medium is considered to be wavelength dependent (see caption for Fig. 6). In single scattering approximation the theoretical model gives the same values of $K_i(\lambda_1, \lambda_2, \vartheta)$ and $K_p(\lambda_1, \lambda_2, \vartheta)$ for both flights with the same ϑ (see Fig. 6). Similar results can be obtained when one considers e.g. single scattering by spheres, chaotically oriented nonspherical mirror symmetric particles.

Fig. 7 presents calculated $K_i(\lambda_1, \lambda_2, \vartheta)$ and $K_p(\lambda_1, \lambda_2, \vartheta)$ on the basis of the vector radiative transfer theory [9,11]. The medium is considered to be a semi-infinite medium of small spherical particles without resonances in the angular dependencies of $F_{21}(\vartheta)$. The size parameters and the refractive indexes of the particles of the medium depend on the wavelength ($x_{\lambda_1} = 1.5$, $m_{\lambda_1} = 1.5$; $x_{\lambda_2} = 1$, $m_{\lambda_2} = 1.6$). The values of viewing angle for these calculations were in the range: $-90^\circ < \vartheta_v < 90^\circ$. Fig. 7 shows different angular dependencies of both $K_i(\lambda_1, \lambda_2, \vartheta)$ and $K_p(\lambda_1, \lambda_2, \vartheta)$ for the different geometries of the two RSP flights which give the same scattering angle ϑ. This difference is due to contribution of multiple scattering. In this case the reflection matrix $\mathbf{R}_{surf}(\lambda, \mathbf{n}_v, \mathbf{n}_{inc})$ and the

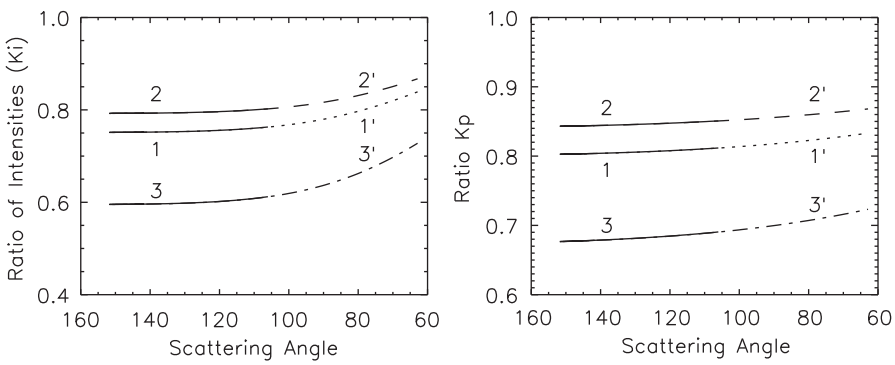

Fig. 6. Angular dependencies of the ratios $K_i(\lambda_1, \lambda_2, \vartheta)$ and $K_p(\lambda_1, \lambda_2, \vartheta)$ within the model with Fresnel reflection by facets [18]. The solid curves 1, 2, 3 correspond to the illumination and scattering geometries of the flight 1. The curves 1′, 2′, 3′ correspond to the geometries of the flight 2 (see Table 1). The curves 1 and 1′ correspond to the ratios when $m_{\lambda_1} = 1.5$, $m_{\lambda_2} = 1.6$; 2 and 2′: $m_{\lambda_1} = 1.6$, $m_{\lambda_2} = 1.7$; 3 and 3′: $m_{\lambda_1} = 1.5$, $m_{\lambda_2} = 1.7$.

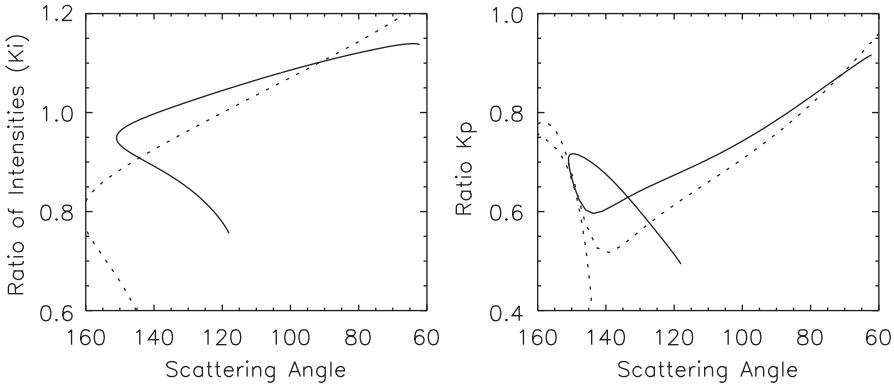

Fig. 7. Angular dependencies of the ratios $K_i(\lambda_1, \lambda_2, \vartheta)$ and $K_p(\lambda_1, \lambda_2, \vartheta)$ obtained from the solution of the vector radiative transfer equation for semi-infinite medium of spherical particles (see description in the text). The solid curve corresponds to the illumination and scattering geometries of the flight 1. The dotted one corresponds to the geometries of the flight 2 (see Table 1).

Stokes parameters of scattered radiation cannot be presented in the simple form described by Eqs. (6)–(9) [9,30].

3.2. A general form for surface reflection models

Let us now consider the ratios K_i and K_p from RSP. Figs. 8 and 9 present the angular dependencies of the ratios $\langle K_i(\lambda_1, \lambda_2, \vartheta)\rangle$ and $\langle K_p(\lambda_1, \lambda_2, \vartheta)\rangle$ obtained from RSP after atmospheric correction and averaging over different scans (see Figs. 4 and 5). Fig. 8 shows the results for soil and Fig. 9 for the vegetation surfaces. Both figures demonstrate good coincidence of the angular dependencies of the intensity ratios $\langle K_i(\lambda_1, \lambda_2, \vartheta)\rangle$ for the considered flights. In particular, for the same type of soil or vegetation surfaces the ratio of total reflectances $\langle K_i\rangle$, taken at two different wavelengths, is almost independent of scattering angle and is the same for different illumination and scattering geometries (for different flights). For example, the flights 1 and 2, 2 and 3, 1 and 4 have different illumination and scattering geometries (see Table 1) but the intensity ratios for them are almost the same (a shift of the curves 1 and 1″, 3 and 3″ in Fig. 9 for the ratio $\langle K_i(\lambda_1, \lambda_2, \vartheta)\rangle$ may be due to the fact that *ARVI* is different for the flights 1 and 4 (see Table 1)). As it was mentioned above, both the dependence of $R_I(\mathbf{n}_v, \mathbf{n}_{inc})$ on the illumination and scattering geometries and independence of $\langle K_i\rangle$ on the geometries are possible when the total reflectance for surfaces can be presented in the following form:

$$R_I(\lambda, \mathbf{n}_v, \mathbf{n}_{inc}) \approx F_I(\lambda, \vartheta) f_I(\mathbf{n}_v, \mathbf{n}_{inc}). \tag{14}$$

Here the function $f_I(\mathbf{n}_v, \mathbf{n}_{inc})$ is still undefined both for soil and vegetation. According to Figs. 8 and 9, it depends on the illumination and scattering geometries but not on the wavelength. The function F_I may be considered as the element F_{11} of a scattering matrix, whose scattering angle dependence may be not considerable in the range $80^\circ \le \vartheta \le 160^\circ$ for visible and short-wave infrared spectral regions.

Let us consider now the angular profiles of $\langle K_p\rangle$ for the different illumination and scattering geometries of the flights from Table 1. Comparing the angular profiles of

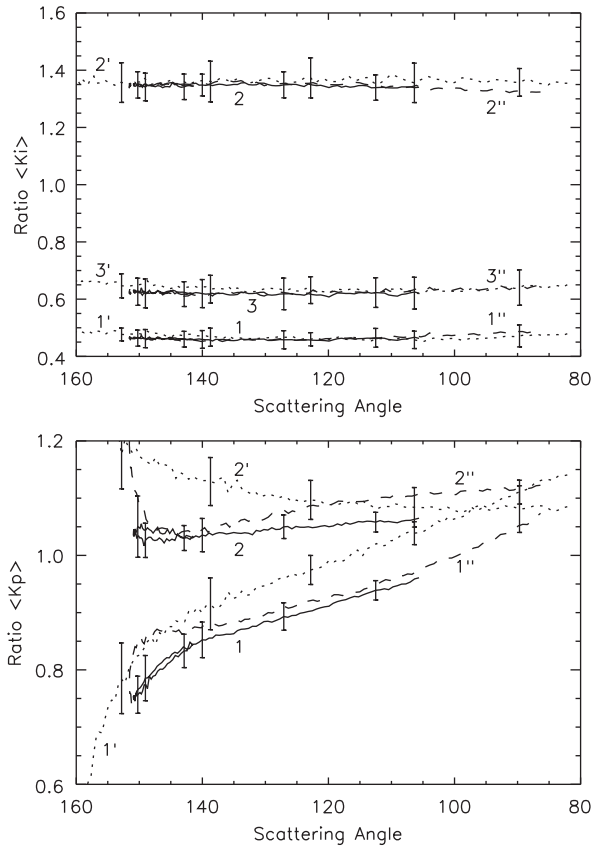

Fig. 8. Angular dependencies of the averaged ratios $\langle K_i(\lambda_1, \lambda_2, \vartheta)\rangle$ and $\langle K_p(\lambda_1, \lambda_2, \vartheta)\rangle$ obtained from RSP measured data for soil. The solid, dotted and dashed curves show the ratios for the flights 1, 2 and 3, respectively (see Table 1). The curves 1, 1′ and 1″ correspond to the ratios with $\lambda_1 = 670$ nm and $\lambda_2 = 1588.86$ nm. The curves 2, 2′ and 2″ correspond to the ratios with $\lambda_1 = 1588.86$ nm and $\lambda_2 = 2264.38$ nm. The curves 3, 3′ and 3″ correspond to the ratios with $\lambda_1 = 670$ nm and $\lambda_2 = 2264.38$ nm. Error bars show the standard deviations from the average values.

$\langle K_p\rangle$ in Figs. 8 and 9 with the angular profiles presented in Fig. 6, one can find out that in the backscattering region ($140^\circ \le \vartheta \le 160^\circ$) the measured angular dependencies of

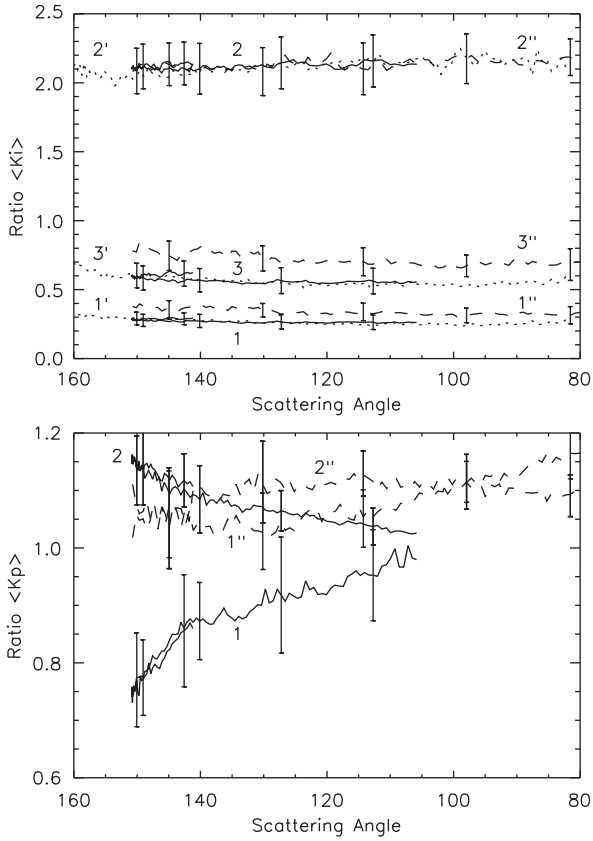

Fig. 9. The same as in Fig. 8 but for vegetation. Curves 1″, 2″ and 3″ correspond to the flight 4 from Table 1.

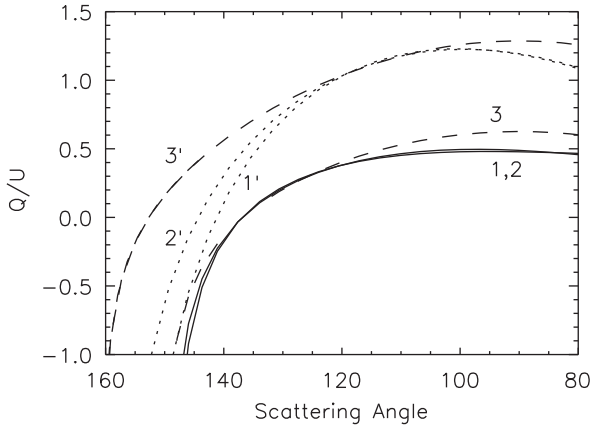

Fig. 10. Angular dependence of the ratio Q/U obtained from the solution of the vector radiative transfer equation for semi-infinite medium of spherical particles. The solid curves correspond to the illumination and scattering geometries for the flight 1. The dotted ones correspond to the geometries for the flight 2. The curves 1 and 1′ correspond to the medium with $x_{\lambda_1}=1.5$, $m_{\lambda_1}=1.5$ and the curves 2 and 2′ correspond to the medium with $x_{\lambda_2}=1$, $m_{\lambda_2}=1.6$. The curves 3 and 3′ represent $\cot 2\eta_v$ for the illumination and scattering geometries for the flights 1 and 2.

$\langle K_p \rangle$ differ from those obtained from the models with Fresnel reflection from surface facets. The fact that Fresnel reflection models have difficulties in the description of the surface polarized reflectance near the backscattering direction was pointed out in number of papers [20,31]. As one can see from Figs. 8 and 9, the agreement on $\langle K_p \rangle$ for the different illumination and scattering conditions is not as well pronounced as on $\langle K_i \rangle$. This may be due to the fact that the considered flights were not carried out completely at the same conditions. The polarized reflectance is more sensitive to differences in the conditions than the total reflectance.

To make a conclusion concerning the models for surface polarized reflectance, let us consider the ratio of the Stokes parameters Q and U, taken for the same flights and for the same wavelength. Within the model described by Eqs. (8) and (9) the ratio of Q and U is independent of the wavelength and equal to $\cot 2\eta_v = \cos 2\eta_v / \sin 2\eta_v$. For more complicated BPDF models the ratio Q/U may differ considerably from $\cot 2\eta_v$. This is demonstrated in Fig. 10 where the angular dependencies of the ratio Q/U, calculated on the basis of the vector radiative transfer theory [9,11], are presented for the same medium as the data in Fig. 7.

Fig. 11 presents the angular dependencies of the ratio Q/U at three different wavelengths for the flights from Table 1. For comparison, Fig. 11 shows also the dependence of $\cot 2\eta_v$ on the scattering angle. Let us consider first the data for soil in Fig. 11. As one can see from Fig. 11, in the range $105^\circ \le \vartheta \le 160^\circ$ the values of $\cot 2\eta_v$ are within the standard deviation from $\langle Q/U \rangle$ obtained in the channels 4, 7 and 9 for flight 1 and in the channels 7, 9 for flight 2. For the flight 2 $\cot 2\eta_v$ may be out of standard deviation from $\langle Q/U \rangle$ in the range $80^\circ \le \vartheta \le 160^\circ$ for the channel 4 and in the range $80^\circ \le \vartheta \le 105^\circ$ for the channels 7, 9. For the flight 2 the relative difference between $\cot 2\eta_v$ and $\langle Q/U \rangle$ may be up to 15% and 7% for the channels 4 and 7, respectively, in the range $80^\circ \le \vartheta \le 135^\circ$. We did not consider the relative difference in the range $140^\circ \le \vartheta \le 160^\circ$ for the flight 2 since in this range the values of Q and U are close to 0.

The data for vegetation show much bigger dispersion than the data for soil. The values of $\cot 2\eta_v$ are within the standard deviation from $\langle Q/U \rangle$ obtained in the channels 4, 7 and 9 both for the flights 1 and 4 (see plots for vegetation in Fig. 11).

The relative difference between $\cot 2\eta_v$ and $\langle Q/U \rangle$ is different for different channels. Thus it cannot be explained by variation of observation angle ϑ_v which would result from a change in aircraft pitch. Such variation should manifest itself similarly in all channels, since the RSP instrument measures the signal in all channels simultaneously [23].

Overall, it can be concluded from Fig. 11 that the simultaneous description of Q and U by Eqs. (8) and (9) can lead to errors up to 15%. However, it is necessary to note that these errors may manifest themselves much less in the polarized reflectance R_P and at the top of atmosphere, thus they may be not essential in the problem of retrieval of aerosol properties over land. Therefore, we conclude that for this purpose the polarized reflectance

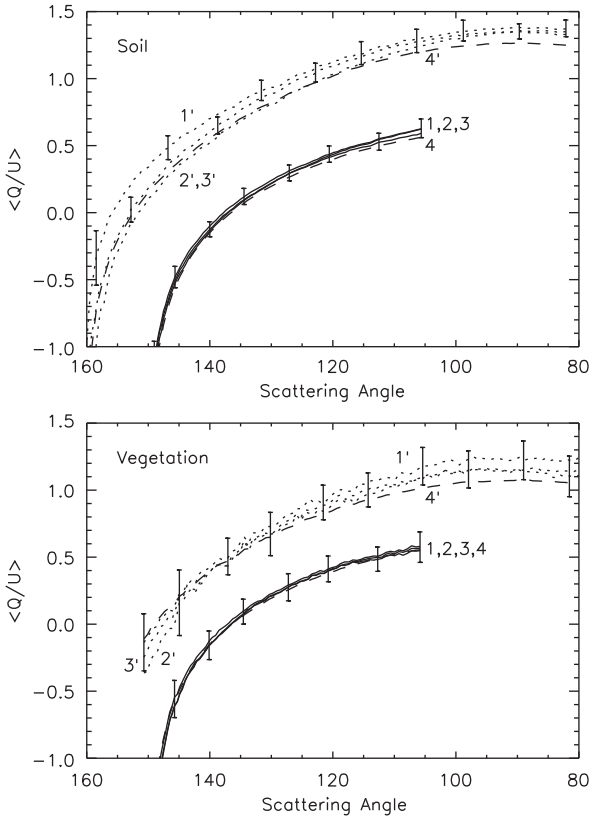

Fig. 11. Angular dependence of the averaged ratio $\langle Q/U \rangle$ for soil and vegetation. For soil the solid and dotted curves are obtained for the flights 1 and 2, respectively. For vegetation the solid and dotted curves are obtained for the flight 1 and 4, respectively (see Table 1). The curves 1 and 1′ correspond to the channel 4; 2 and 2′: to the channel 7; 3 and 3′: to the channel 9. The curves 4 and 4′ represent $\cot 2\eta_v$ for the illumination and scattering geometries of the flights 1 and 2 (for soil) and of the flights 1 and 4 (for vegetation), respectively. Error bars show the standard deviations from the average values.

from soil and vegetation may be approximated by

$$R_Q(\lambda, \mathbf{n}_v, \mathbf{n}_{inc}) \approx F_P(\lambda, \vartheta) f_P(\mathbf{n}_v, \mathbf{n}_{inc}) \cos 2\eta_v, \tag{15}$$

$$R_U(\lambda, \mathbf{n}_v, \mathbf{n}_{inc}) \approx F_P(\lambda, \vartheta) f_P(\mathbf{n}_v, \mathbf{n}_{inc}) \sin 2\eta_v. \tag{16}$$

Here, similarly to Eq. (14), the function $f_P(\mathbf{n}_v, \mathbf{n}_{inc})$ is a wavelength independent function of the illumination and scattering geometries. It is defined by the model which is used to describe polarization of scattered radiation and may differ from $f_I(\mathbf{n}_v, \mathbf{n}_{inc})$ in Eq. (14). The function F_P may be considered as the element F_{21} of a scattering matrix.

4. Discussion

Figs. 8 and 9 show that the ratio $\langle K_i \rangle$ is independent of the scattering angle. This finding may be important for satellite aerosol retrievals over land. It demonstrates that the surface total reflectance depends almost linearly on the wavelength dependent models parameter (see, Eq. (14) with $F_I(\lambda, \vartheta) \approx const(\lambda)$). Moreover, it suggests that it is possible to retrieve the wavelength independent part of surface reflectance model from measurements in the short-wave infrared range where, in general, the aerosols effect on the measurement is small. A similar method has been used by Waquet et al. [22] to retrieve surface polarized reflectance.

Virtual independence of F_I on the illumination and scattering geometries allows one also to consider in details the function $f_I(\mathbf{n}_v, \mathbf{n}_{inc})$ from Eq. (14). In this case one can write for the reflectance:

$$R_I(\lambda, \mathbf{n}_v, \mathbf{n}_{inc}) \approx a_0(\lambda) f_I(\mathbf{n}_v, \mathbf{n}_{inc}), \tag{17}$$

where $a_0(\lambda)$ can be considered as the average value of $F_I(\lambda, \vartheta)$ in the range $80^\circ \le \vartheta \le 160^\circ$ at given λ ($a_0(\lambda) \approx \langle F_I(\lambda, \vartheta) \rangle$). The function $f_I(\mathbf{n}_v, \mathbf{n}_{inc})$ can be presented in the following form:

$$f_I(\mathbf{n}_v, \mathbf{n}_{inc}) = f_{sh}(\mathbf{n}_v, \mathbf{n}_{inc}) f_I^{mod}(\mathbf{n}_v, \mathbf{n}_{inc}), \tag{18}$$

where $f_{sh}(\mathbf{n}_v, \mathbf{n}_{inc})$ is a shadowing function and the function $f_I^{mod}(\mathbf{n}_v, \mathbf{n}_{inc})$ is defined by the model for surface total reflectance. For example, in the solution of the radiative transfer equation for semi-infinite media the function $f_I^{mod}(\mathbf{n}_v, \mathbf{n}_{inc})$ may be presented as [9]

$$f_I^{mod}(\mathbf{n}_v, \mathbf{n}_{inc}) = \frac{1}{\cos\vartheta_v + \cos\vartheta_{sol}}, \tag{19}$$

where ϑ_v and ϑ_{sol} are viewing and solar zenith angles.

Fig. 12 shows the angular profiles of the normalized function $f_{sh}(\mathbf{n}_v, \mathbf{n}_{inc})$ obtained from RSP photometric measurements using Eqs. (17)–(19) with $R_I(\lambda, \mathbf{n}_v, \mathbf{n}_{inc})$ equal to the measured total reflectance averaged over different scans. As one can see from Fig. 12 the function $f_{sh}(\mathbf{n}_v, \mathbf{n}_{inc})$ behaves as a shadowing function with a maximum for the scattering angle whose value is the closest to 180°. It depends not just on the scattering angle but also on the difference of the azimuth angles of incidence and viewing directions and solar zenith angle. Qualitatively, the dependence of this function on the illumination and scattering geometries is similar to the dependence of the shadowing function modeled for Gaussian and fractal-like rough surfaces (see, for example, [32]).

Shadowing effects must manifest themselves both in photometric and polarimetric characteristics of scattered radiation. In other words, for the function $f_P(\mathbf{n}_v, \mathbf{n}_{inc})$ from Eqs. (15) and (16) one can write:

$$f_P(\mathbf{n}_v, \mathbf{n}_{inc}) = f_{sh}(\mathbf{n}_v, \mathbf{n}_{inc}) f_P^{mod}(\mathbf{n}_v, \mathbf{n}_{inc}), \tag{20}$$

where the function $f_{sh}(\mathbf{n}_v, \mathbf{n}_{inc})$ is the same as in Eq. (18) but the function $f_P^{mod}(\mathbf{n}_v, \mathbf{n}_{inc})$ is defined by the model for surface polarized reflectance, and may differ from $f_I^{mod}(\mathbf{n}_v, \mathbf{n}_{inc})$. For example, within the Fresnel models for polarization $f_P^{mod}(\mathbf{n}_v, \mathbf{n}_{inc})$ may contain the probability density function for the slopes at the surface and has different dependence on the illumination and scattering geometries than $f_I^{mod}(\mathbf{n}_v, \mathbf{n}_{inc})$ within the kernel-driven models [1,13–22].

Let us note that when physically different models are used for the description of the total and polarized reflectances it is difficult to make a reliable assumption concerning the angular and spectral dependencies of other elements of the reflection matrix (for example, R_{22}^{surf}, R_{33}^{surf}, etc.) on the basis of measurements for the case

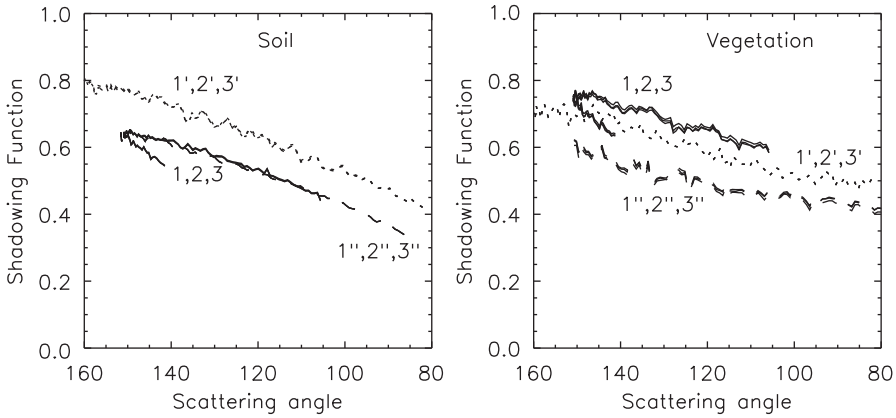

Fig. 12. Normalized shadowing function for soil and vegetation obtained from photometric RSP measurements. For soil the solid, dotted and dashed curves are obtained for the flights 1, 2 and 3, respectively. For vegetation the solid, dotted and dashed curves are obtained for the flights 1, 2 and 4, respectively (see Table 1). The curves 1, 1′ and 1″ are obtained for $\lambda = 670$ nm; 2, 2′ and 2″: for $\lambda = 1588.86$ nm; 3, 3′ and 3″: for $\lambda = 2264.38$ nm.

of unpolarized incident radiation. Often it is necessary to know all elements of the reflection matrix. This is the case, for example, in the problem of aerosol properties retrieval over land, where transfer of polarized radiation in coupled atmosphere–surface system is considered. Importance of this aspect for aerosol properties retrieval over land still has to be estimated.

As one can see from Figs. 4, 5 and 8, 9, there is a small difference in surface polarized reflectance between the channels 4 and 7. Thus if one assumes that surface polarized reflectance is spectrally independent between the short-wave infrared and the red bands, a small error δ_p is introduced in the degree of linear polarization in the channel 4 ($\delta_p = (R_P(\lambda_1) - R_P(\lambda_2))/R_I(\lambda_1) * 100\%$, where $R_P(\lambda_1)$ and $R_P(\lambda_2)$ are the polarized reflectances in the channels 4 and 7, respectively, $R_I(\lambda_1)$ is the total reflectance in the channel 4). For the data presented in Fig. 4 this error is of the order of 0.1–0.8% in the range $95^\circ \le \vartheta \le 160^\circ$. For aerosol retrievals it is important to estimate this effect at the top of the atmosphere. The assumption of spectrally independent surface polarized reflectance leads to a forward model error at the top of the atmosphere of the order of 0.1–0.6% for an aerosol optical thickness 0.04 and of the order of 0.1–0.3% for the aerosol optical thickness 0.35 (for both cases $95^\circ \le \vartheta \le 160^\circ$). If we compare these values with the 0.2% polarimetric accuracy of Glory-APS, it follows that wavelength dependence of surface polarization may be important to take into account when the aerosol optical thickness is small.

Let us note also that the observed spectral dependence of the polarized reflectance cannot be explained within the model based on single Fresnel reflection. It may be due to volume scattering inside leaves or soil particles which is responsible for strong spectral dependence of the total reflectance.

5. Summary

In this paper we have shown on the basis of the analysis of photopolarimetric RSP data that both for soil and vegetation surfaces the models for total and polarized reflectances can be presented in the same form: as a product of a geometrical scattering term and a term depending on the wavelength and the scattering angle (see Eq. (14)–(16)). The geometric scattering term ($f_I(\mathbf{n}_v, \mathbf{n}_{inc})$ and $f_P(\mathbf{n}_v, \mathbf{n}_{inc})$) depends just on the illumination and viewing conditions, whereas the wavelength dependent term ($F_I(\lambda, \vartheta)$ and $F_P(\lambda, \vartheta)$) is the same for different illumination and scattering geometries corresponding to the same scattering angle. Thus both for soil and vegetation surfaces the multiple scattering either contributes slightly to the BDRF and BPDF in comparison with the single scattering contribution or its contribution does not change considerably the dependence on the illumination and viewing geometry.

The RSP measurements in the 'red' ($\lambda = 670$ nm) and in the 'short-wave infrared' ($\lambda = 1589$ nm) bands show a small wavelength dependence of polarized reflectance for soil and vegetation surfaces. With increasing atmospheric optical thickness the spectral dependence of the surface polarized reflectance will manifest itself less at the top of atmosphere but may be important for small values of the optical thickness. More detailed analysis of surface polarized reflectance spectral variability still has to be carried out over a more diverse sample of surfaces.

It was found both for soil and vegetation surfaces that the ratio $\langle K_i \rangle$ of the total reflectances taken at two different wavelengths from visible and short-wave infrared regions is the same for different illumination and scattering geometries and independent of the scattering angle (see Figs. 8 and 9). This finding may be important for the problem of aerosol properties retrieval over land.

Acknowledgments

We are grateful to K. Knobelspiesse for useful discussions. We also thank anonymous reviewers for their useful comments which helped to improve the paper. This research was supported by the Dutch User Support Program (USP) under project GO-AO/03.

Appendix A. Total reflectance and polarized reflectance. Illumination and scattering geometry

A.1. Definition of total and polarized reflectances

The total reflectance R_I and polarized reflectances R_Q, R_U, R_P can be defined as

$$R_I = \frac{I}{F_0|\cos\vartheta_{inc}|}, \tag{21}$$

$$R_Q = \frac{Q}{F_0|\cos\vartheta_{inc}|}, \tag{22}$$

$$R_U = \frac{U}{F_0|\cos\vartheta_{inc}|}, \tag{23}$$

$$R_P = \frac{\sqrt{Q^2+U^2}}{F_0|\cos\vartheta_{inc}|}, \tag{24}$$

where I, Q and U are the Stokes parameters of scattered radiation, ϑ_{inc} is the zenith incident angles, πF_0 is the incident flux per unit area perpendicular to the incident beam.

A.2. Illumination and scattering geometry

In Fig. A1 the angles of illumination and scattering geometries are presented. During the ALIVE measurements the solar azimuth φ_{sol} and azimuth of viewing directions φ'_v were counted off the direction to Earth North Pole. In our calculations we used azimuth angles of incident and viewing directions (φ_{inc} and φ_v) counted off the direction to Earth South Pole (see Fig. A1).

The scattering angle ϑ is defined in the scattering plane (the plane containing the vectors $\mathbf{n}_{inc}$ and $\mathbf{n}_v$) as the angle between the vectors $\mathbf{n}_{inc}$ and $\mathbf{n}_v$ (see Fig. A1):

$$\cos\vartheta = \cos\vartheta_v\cos\vartheta_{inc} + \sin|\vartheta_v|\sin\vartheta_{inc}\cos(\varphi_v - \varphi_{inc}), \tag{25}$$

where ϑ_{inc}, ϑ_v are zenith incident, zenith viewing angles, respectively ($\vartheta_{inc} = \pi - \vartheta_{sol}$, ϑ_{sol} is solar zenith angle (see Fig. A1 and Table 1); $-40^\circ \le \vartheta_v \le 60^\circ$), φ_{inc}, φ_v are azimuth angles of incident and viewing directions ($\varphi_{inc} = 2\pi - \varphi_{sol}$, φ_{sol} is solar azimuth angles from measurements (see Fig. A1 and Table 1); $\varphi_v = 2\pi - \varphi'_v$ for $\vartheta_v < 0$ and $\varphi_v = \pi - \varphi'_v$ for $\vartheta_v \ge 0$ (φ'_v is azimuth of viewing directions from measurements (observation azimuth, see Fig. A1 and Table 1)).

The dihedral angle η_v, which is the angle between the scattering plane and the plane containing axis z of the reference coordinate system and the vector $\mathbf{n}_v$, can be defined, for example, from the equation [30]

$$\cos\eta_v = \frac{\cos\vartheta_{inc} - \cos\vartheta_v\cos\vartheta}{\sin|\vartheta_v|\sin\vartheta}. \tag{26}$$

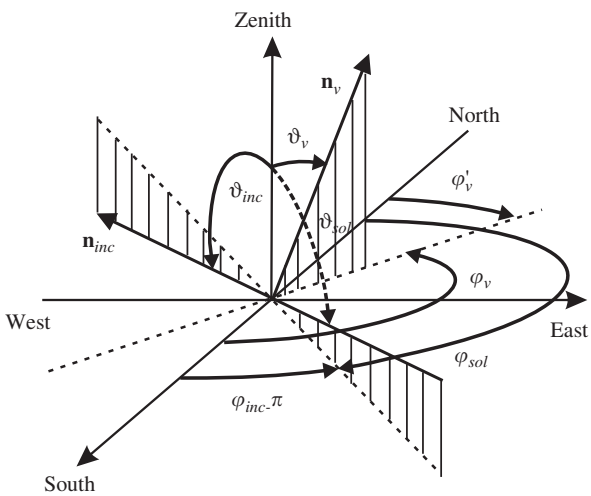

Fig. A1. Illumination and scattering geometry.

References

[1] Tsang L, Kong JA, Shin RT. Theory of microwave remote sensing. New York: Wiley; 1985.
[2] Tsang L, Kong JA, Ding K-H. Scattering of electromagnetic waves: theories and applications. New York: Wiley; 2000.
[3] Tsang L, Kong JA, Ding K-H. Scattering of electromagnetic waves. Advanced topics. New York: Wiley; 2001.
[4] Tishkovets VP, Petrova EV, Jockers K. Optical properties of aggregate particles comparable in size to the wavelength. JQSRT 2004;86: 241–65.
[5] Nousiainen T, Muinonen K, Raisanen P. Scattering of light by large Saharan dust particles in a modified ray optics approximation. J Geophys Res 2003;108(D1):4025.
[6] Munoz O, Volten H, Hovenier JW, Nousiainen T, Muinonen K, Guirado, D, et al. Scattering matrix of large Saharan dust particles: experiments and computations. J Geophys Res 2007;112:D13215.
[7] Jacquemound S, Baret F. PROSPECT: a model of leaf optical properties spectra. Remote Sensing Environ 1990;34:75–91.
[8] Muinonen K, Nousiainen T, Lindqvist H, Munoz O, Videen G. Light scattering by Gaussian particles with internal inclusions and roughened surfaces using ray optics. JQSRT 2009;110:1628–39.
[9] Mishchenko MI, Travis LD, Lacis AA. Multiple scattering of light by particles. Radiative transfer and coherent backscattering. Cambridge: Cambridge University Press; 2006.
[10] Tishkovets VP, Jockers K. Multiple scattering of light by densely packed random media of spherical particles: dense media vector radiative transfer equation. JQSRT 2006;101:54–72.
[11] Mishchenko MI, Dlugach JM, Yanovitskij EG, Zakharova NT. Bidirectional reflectance of flat, optically thick particulate layers: an efficient radiative transfer solution and applications to snow and soil surfaces. JQSRT 1999;63:409–32.
[12] Hasekamp OP, Landgraf J. Retrieval of aerosol properties over land surfaces: capabilities of multiple-viewing-angle intensity and polarization measurements. Appl Opt 2007;46(16):3332–44.
[13] Hapke B. Bidirectional reflectance spectroscopy 1. Theory. J Geophys Res 1981;86(B4):3039–54.
[14] Roujean J-L, Leroy M, Deschamps P-Y. A bidirectional reflectance model of the Earth's surface for the correction of remote sensing data. J Geophys Res 1992;97(D18):20455–68.
[15] Wanner W, Li X, Strahlar AH. On the derivation of kernals for kernel-driven models of bidirectional reflectance. J Geophys Res 1995;100(D10):21077–89.
[16] Rahman H, Pinty B, Verstraete MM. Coupled surface–atmosphere reflectance (CSAR) model 2. Semiempirical surface model usable with NOAA advanced very high resolution radiometer data. J Geophys Res 1993;98(D11):20791–801.
[17] Spurr RJD. A new approach to the retrieval of surface properties from earthshine measurements. JQSRT 2004;83:15–46.
[18] Mishchenko MI, Travis LD. Satellite retrieval of aerosol properties over the ocean using polarization as well as intensity of reflected sunlight. J Geophys Res 1997;102:16989–7013.
[19] Rondeaux G, Herman M. Polarization of light reflected by crop canopies. Remote Sensing Environ 1991;38:63–75.
[20] Breon F-M, Tanre D, Lecomte P, Herman M. Polarized reflectance of bare soil and vegetation: measurements and models. IEEE Trans Geosci Remote Sensing 1995;33:487–99.
[21] Waquet F, Leon J-F, Cairns B, Goloub P, Deuze J-L, Auriol F. Analysis of the spectral and angular response of the vegetated surface polarization for the purpose of aerosol remote sensing over land. Appl Opt 2009;48(6):1228–36.

[22] Waquet F, Cairns B, Knobelspiesse K, Chowdhary J, Travis LD, Schmid, B, et al. Polarimetric remote sensing of aerosols over land. J Geophys Res 2009;114:D01206.
[23] Cairns B, Russel EE, Travis LD. The research scanning polarimeter: calibration and ground-based measurements. Proc SPIE 1999;3754: 186.
[24] Mishchenko M, Cairns B, Kopp G, Schueler G, Fafaul C, Hansen, J, et al. Accurate monitoring of terrestrial aerosols and total solar irradiance: introducing the Glory mission. Bull Amer Meteorol Soc 2007:88.
[25] Knobelspiesse KD, Cairns B, Schaaf CB, Schmid B, Roman MO. Surface BDRF estimation from an aircraft compared to MODIS and ground estimates at the Southern great plains site. J Geophys Res 2008;113:D20105.
[26] Kaufman YJ, Tanre D. Atmospherically resistant vegetation index (ARVI) for EOS-MODIS. IEEE Trans Geosci Remote sensing 1992;30:261–70.
[27] Hasekamp OP, Landgraf J. Linearization of vector radiative transfer with respect to aerosol properties and its use in satellite remote sensing. J Geophys Res 2005;110:D04203.
[28] Hasekamp OP, Landgraf J. A linearized vector radiative transfer model for atmospheric trace gas retrievals. JQSRT 2002;75:221–38.
[29] Stier P, Feichter J, Kinne S, Kloster S, Vignati E, Wilson, J, et al. The aerosol-climate model ECHAM5-HAM. Atmos Chem Phys 2005: 1125–56.
[30] Hovenier JW, Van der Mee C, Domke H. Transfer of polarized light in planetary atmospheres. Dordrecht: Kluwer academic Publishers; 2004.
[31] Elias T, Cairns B, Chowdhary J. Surface optical properties measured by the airborne research scanning polarimeter during the CLAMS experiment. Proc SPIE 2004;5235:595–606.
[32] Parviainen H, Muinonen K. Rough-surface shadowing of self-affine random rough surfaces. JQSRT 2007;106:398–416.